Hybrid metal-ceramic biomaterials fabricated through powder bed fusion and powder metallurgy for improved impact resistance of craniofacial implants

Ramin Rahmani [a,b,c,*], Nikhil Kamboj [a,d], Miha Brojan [b], Maksim Antonov [a], Konda Gokuldoss Prashanth [a,e,f]

[a] Department of Mechanical and Industrial Engineering, Tallinn University of Technology, Ehitajate tee 5, 19086 Tallinn, Estonia
[b] Laboratory for Nonlinear Mechanics, Faculty of Mechanical Engineering, University of Ljubljana, Aškerčeva cesta 6, SI, 1000 Ljubljana, Slovenia
[c] Centre of Advanced Manufacturing Technologies, Łukasiewicz Research Network, Krakow Institute of Technology, Zakopiańska 77, 30-418 Kraków, Poland
[d] Turku Clinical Biomaterials Centre (TCBC), Department of Biomaterials Science, Faculty of Medicine, Institute of Dentistry, University of Turku, FI, 20014, Turku, Finland
[e] CBCMT, School of Mechanical Engineering, Vellore Institute of Technology, 632014, Tamil Nadu, India
[f] Erich Schmid Institute of Materials Science, Austrian Academy of Science, Jahnstraße 12, A-8700 Leoben, Austria

ARTICLE INFO

ABSTRACT

The mechanical compliance of craniofacial implants is of paramount importance in the medical field, as the primary concern is to protect the cerebrum after trauma or neurosurgical operation. To develop novel cranial implants, three types of bioactive ceramic powders were embedded in the metallic scaffolds. The scaffolds were fabricated by combining powder bed fusion technology and powder metallurgy. Ti6Al4V lattice structures fabricated by selective laser melting were filled with three different wollastonite-based bioceramics applied for critical-sized craniofacial defects: 1. $CaSiO_3$ (wollastonite, W), 2. $Si-CaSiO_3$ (50 wt.% silicon-wollastonite, W-Si) and 3. $CaSiO_3\_Ca_3(PO_4)_2\_MgCa(SiO_3)_2$ (62 wt.% wollastonite ceramic glass, W62) by spark plasma sintering. The mechanical behavior of the $Ti6Al4V-CaSiO_3$ hybrid metal-ceramic biomaterial composite was evaluated by the dynamic impact test designed by the authors. Furthermore, the proposed fabrication process implies that the metallic scaffolds can bear the mechanical loads, hold the composite structure together, and deliberately induced cracks/pores in the ceramic region can be exploited for drug delivery. Except Ti6Al4V which is known for implants, the potential of using TiNi and Ti22Al25Nb is investigated here for dynamic impact-resistance applications. Due to ductility of TiNi and rigidity of Ti22Al25Nb, an average stress distributed in structures under loading is approximately 600, 550 and 400 MPa for Ti6Al4V, TiNi, and Ti22Al25Nb, respectively. Results show declination in the level of porosity from ceramic (W) to metalloid-ceramic (W-Si) and ceramic-glass (W62) in the composite, respectively, and limited cracking in the impact region of the ceramic and the metallic struts interface when subjected to multiple dynamic impacts.

1. Introduction

Inspired by biology, many modern advanced composites exhibit high strength, high toughness, and high impact resistance properties [1,2]. With the advent of these materials, the fabrication routes of synthetic materials that mimic biological materials have become a thriving area of research [3,4]. These bio-inspired materials can also be homologous to meta-biomaterials [5,6]. Synthetic biomaterials replicating bone structures should have alluring toughening mechanisms especially in bone-related applications, as bone displays crack deflection, crack bridging, and microcracking [7–9]. At the nanoscale, the geometric design of the biomaterial nanopatterns could facilitate the final shape of the meta-biomaterial into a complex three-dimensional shape which is henceforth capable of imparting mechanical properties, like in auxetic and origami-inspired meta-materials [10,11]. Mechanical properties include fatigue behavior, quasi-state mechanical properties, and impact resistance properties. Microscale meta-biomaterials could improve the performance in two ways: first, additive manufacturing (AM) of scaffolds or triply periodic minimal surface (TPMS) biomaterials are generally known to have a higher surface area when collated with the solid counterpart which could have several effects on improving the osteogenic response, and second, the internal pore space to assist the carrying of drug-delivery vehicles, stem cells and growth factors [12–14]. However, to the best

---

* Corresponding author.
 E-mail address: ramin.rahmaniahranjani@gmail.com (R. Rahmani).

knowledge of the authors, no study in the literature explains the concept of hybrid biomaterials, which include the bioceramic component at the micro level to improve the performance in periodic dynamic impacts. This type of solution could be used in trauma surgery, e.g. for craniofacial implants.

Cranial implants are usually fabricated from bio-inert materials like PMMA and titanium alloys. To improve the performance of the implant, it is recommended by several authors to add bioactive elements, osteoconductive materials, or bioactive glass fibers to enhance the osseointegration and helps to accelerate the angiogenesis process [15–17]. It is well known that no permanent load acts on the cranial implant, which is why it is therefore regarded as a non-loaded implant. Nevertheless, most studies on cranial implants are dedicated to quasi-static compression loading, usually by an indenter [18–20]. However, more realistic loading conditions, i.e. dynamic impact loading, should be established for testing the cranial implant. To the best of the authors' knowledge, there are only a few studies dedicated to the investigation of cranial implants under impact loading, see e.g. [21,22]. Lewin et al. fabricated calcium phosphate-titanium cranial implants with the peak load ranging from 808 to 852 N. Matic et al. fabricated titanium mesh like a cup, filled with a thick layer of HA with a peak load of 1200 N for the impact test to resist the fracture. Cranial implants are commonly fabricated from bio-inert materials like titanium-based materials and polymers. An improved outcome can be obtained by including bioactive elements in the implants which can mitigate the potential adverse effects at the implant site such as infection and immune rejection. Therefore, in this study, bioceramic components with three different powders were embedded in a metallic scaffold to potentially improve osseointegration and vascularization at the defect site. With the increase in demand for patient-specific implants to protect the cerebrum, the mechanical response, especially under impact loading, requires more attention.

Powder bed fusion (PBF) techniques include a wide range of methods such as selective laser sintering (SLS), selective laser melting (SLM), and electron beam melting (EBM) to produce dense metallic and ceramic structures. PBF/AM is a technology for additive layer-by-layer fabrication of the near-net-shape structures from CAD models and offers great potential for prototyping with flexible feedstock and complex geometries [23]. SLM process is known as the most popular laser powder bed fusion (L-PBF) technology and the terminology is standardized as ASTM F2792 for additive manufacturing. Selective laser melting (SLM), as the main subset of AM technology, is based on incremental layer-by-layer manufacturing, where parts are created by melting powdered materials with a laser beam source in a build chamber to form a solid. Powders of different sizes and flowability can be deposited manually or with a hopper into a built platform over which the material is uniformly spread with a wiper/recoater, [24–26]. Low-density Ti6Al4V alloy is recognized as the most popular $\alpha + \beta$ titanium alloy and spherical powder for 3D printing with high strength, high fracture toughness, high corrosion resistance, and high biocompatibility. Other titanium alloys suitable for both 3D printing and bio-applications are TiNi (Nitinol) and Ti22Al25Nb, which have high corrosion resistance, low density, and high strength, similar to Ti6Al4V. Hence, intensive efforts are being done to substitute Ti-6Al-4 V alloy with V-free titanium alloys for biomedical applications. For these reasons, Ti-6Al-7Nb and Ti-5Al-2.5Fe have been developed and studied. Another technological process we use in our research is spark plasma sintering (SPS), which is based on a direct, pulsed or alternating current passing through the powder. Since it is a rapid process, it enables very high heating/cooling rates. By optimizing the SPS parameters, densified sample with the desired geometry can be achieved in a short time and with low energy consumption. It should be noted that modern powder metallurgy (PM) techniques like SPS allow the reduction of grain growth (due to simultaneous compression and heating as well as short production time), resulting in improved densification and mechanical properties [27,28]. Therefore, a combination of AM and PM approaches can lead to the fabrication of samples

with advanced performance in a wide range of technologies, such as hybrid meta-biomaterials [29,30].

The objective of this study is the design of hybrid bio-metal-ceramic for craniofacial implants using powder bed fusion and powder metallurgy combined techniques. Metallic lattice particularly bears the impact or compression loading since embedded ceramic lixiviate to the body fluid, induce bone formation in the defected area or delivery the antibiotic. In this study, a novel hybrid metal-ceramic biomaterial with increased impact resistance for improved craniofacial implants is presented. The novel aspect of the current study is the application of various material combinations (ranging from metal to ceramic-metal and glass-ceramic-metal), production methods (combined selective laser melting and spark plasma sintering), and impact testing (multiple strikes for measuring the dynamic hardness, impact damping, etc.). The idea is based on fabricating first the metallic scaffold by SLM process, and then by the addition of the bioceramic powders into the spaces and pores of the unit cells of the metallic scaffolds by SPS. The biological significance of the scaffolds prepared this way can be attributed to the lixiviation of the bioceramic powder from the scaffold in simulated body fluids, thereby promoting the activation of early osteogenic genes. At the same time, the metallic scaffold still holds the fracture site which can be considered crucial for cranial defects of critical size (usually larger than 20 mm). The mechanical characterization of scaffolds and hybrid composites is carried out by finite element analysis and experimental tests. It is of great interest to perform numerical simulations of metallic scaffolds during mechanical loading to evaluate different Ti-based alloys with different compositions, densities, etc., and to compare these results with the experimental results of the impact test.

2. Materials and methods

2.1. SLM process

Scanning electron microscopy (SEM) micrographs of titanium-balanced, pre-alloyed and gas-atomized powders Ti6Al4V (Al_6 and V_4 at%, 4.43 g/cm^3, supplied by *SLM Solution AG*, [31]), TiNi (Nitinol, Ni_{50} at%, 6.45 g/cm^3, supplied by *TLS Technik GmbH*, [32]) and Ti22Al25Nb (Al_{22} and Nb_{25} at%, 5.35 g/cm^3, supplied by *Sino-Euro Ltd.* [33]) are shown in Fig 1. These Ti-balanced materials display several auspicious properties, such as: i) Ti6Al4V has exceptional biocompatibility and corrosion resistance, is excellent for 3D printing of complex geometries, e.g. triply periodic minimal surfaces and controlled architectures [34]; ii) Ti-Ni exhibits super-elasticity, shape-memory effect and fatigue resistance, which attracts much interest for potential 4D printing [35]; and iii) Ti-Al-Nb alloy (e.g. Ti2AlNb or Ti22Al25Nb) has high specific strength and high-temperature strength, facilitates high compression and tensile strength at lower cost and process time [36].

A 3D printer *Realizer SLM®280* device (*SLM solutions AG*) with selected optimized exposure time of 25 μs, 25 μm point distance, 2500 mA laser current (laser power: 60 W and scan speed: 1000 mm/s), 60 μm hatch space, and layer thickness of 50 μm with argon gas flow inside the build chamber was applied to fabricate Ti6Al4V lattice/scaffold with $2 \times 2 \times 2$ mm unit cell size, 0.5 mm strut diameter and 16 mm height (see Fig. 2).

2.2. SPS process

Using the SPS process we introduce wollastonite (calcium silicate, W) into the vacant spaces of metallic scaffolds. Because of the bioactivity of the wollastonite, this ceramic phase can induce early osteogenic activity. Bioceramic scaffolds have a potential to be covered by polycaprolactone coatings or embedded in hybrid lattices for vancomycin delivery (see Fig. 3A) [37,38]. Si-CaSiO$_3$ (W-Si) is prepared by mixing powder feedstock of 50 wt.% of silicon (supplied by *Silgrain-Elkem*, size 10–44 μm) and 50 wt.% of wollastonite (supplied by NYCD, designated M1250, size 2–10 μm) for SPS (PM) process. After mixing with ethanol
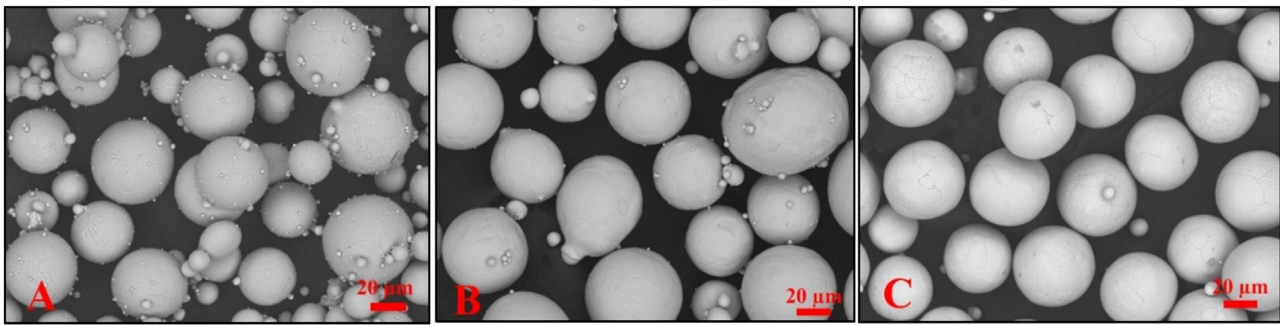
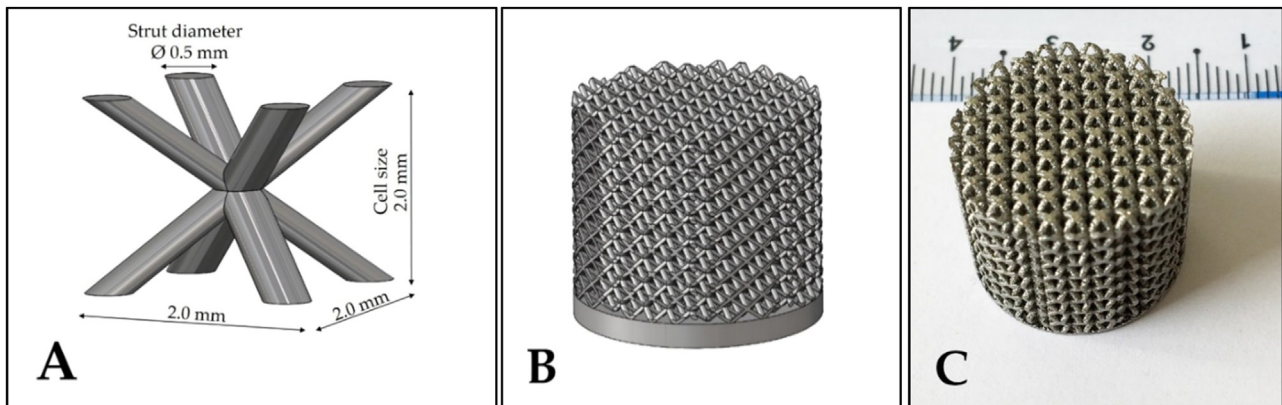Fig. 1. SEM images of spherical powders of titanium alloys: A) Ti6Al4V, B) TiNi, C) Ti22Al25Nb.

Fig. 2. CAD model of: A) Unit cell size with four cross-sectional struts BCC configuration, B) Lattice structure, and C) Ti6Al4V lattice structures fabricated by SLM process. The height of the scaffold after printing is 16 mm (8 unit cells on top of each other) and volume fraction of metallic part is ≈ 40% (after blasting by nanoparticles to remove the sticked/unmelted powders). The diameter is 20 mm and the weight is approximately 4 g after printing, brief polishing and air blasting. There is a solid disk/spacer at the bottom of the structure (usually in the range of 0.1–0.5 mm height) for the connection of lattice cells to the structure support and the 3D printer platform/baseplate.
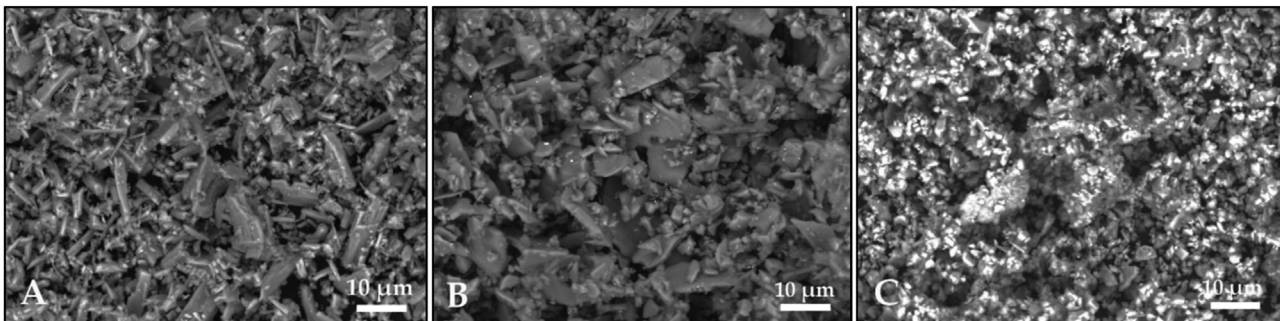

Fig. 3. SEM micrographs of biomaterial powders: A) $CaSiO_3$ (wollastonite, calcium silicate, W), B) $Si-CaSiO_3$ (50–50 wt.% silicon-wollastonite, W-Si), and C) $CaSiO_3\_Ca_3(PO_4)_2\_MgCa(SiO_3)_2$ (62 wt.% wollastonite ceramic glass, W62).

and zirconia balls for 3 h, the mixture is dried and heated for 24 h in an oven. In this way, W-Si, an efficient bioceramic for combined bioactivity and osteoinductivity, is obtained (see Fig. 3B) [39,40]. Another wollastonite component is $CaSiO_3\_Ca_3(PO_4)_2\_MgCa(SiO_3)_2$ (W62, 62 wt.% wollastonite glass ceramic prepared according to the ternary phase diagram of $CaSiO_3\_Ca_3(PO_4)_2\_CaMg(SiO_3)_2$) prepared with the medium particle size of approximately 2.5 μm, synthesized in the laboratory. The glass-ceramic was prepared from 70 vol.% of ceramic and 30 vol.% of glass. The 62 wt.% wollastonite ceramic glass was prepared from

a mixture of reagent grade $CaCO_3$ (98.5–100 wt.% *Merck KGaA, Ref. 1.02066*), SiO_2 (99.7 wt.%, *Strem Chemicals Inc. Ref. 93–1435*), MgO (97 wt.% *Merck KGaA, Ref. 1.05865*) and $Ca_3(PO4)_2$ (Pharma grade, *PanReac AppliChem, Ref. 141,228*). The subsequent mixture was melted in Pt-Rh 10% crucible at 1500 °C in an electric furnace for a total of 2 h, and cold water was poured over it, obtaining a fritted glass. The XRF analysis of the bioactive ceramic-glass is studied in detail in [41]. The novel glass was prepared with the aim of having a broader bioresorbable/biodegradable wollastonite phase in the final composition of
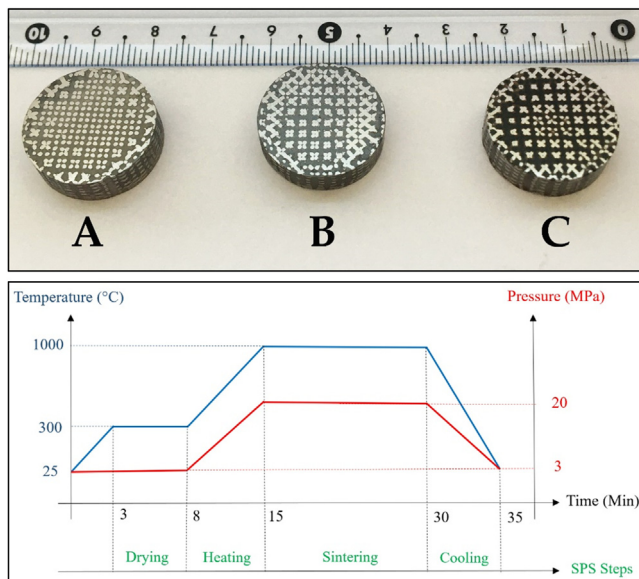
Fig. 5. Laboratory test device equipped by impactor and monitoring system.

Fig. 4. Top: Metal-ceramic samples produced by SPS: A) W (opaque white color), B) W-Si (opaque gray color) and C) W62 (opaque brown color). The used SLM printed Ti6Al4V scaffolds have 20 mm diameter, 2.0 mm unit cell size, 0.5 mm strut diameter and $\approx$ 40% volume fraction before compression; They had a 16 mm of height but shrank to a final height of approximately 6–8 mm after compression during sintering in SPS. Samples were polished by a sandpaper grade P800 for finer surface and removal of the graphite sheet from both sides of disks. The *diamond-type* metallic lattice is chosen to damp the impacts and due to continuity of struts, helps to the increased fracture toughness of the ceramic-metal composite. **Bottom:** SPS temperature-pressure-time sequence.

the glass, which can be easily lixiviated out from the metallic scaffold, thus improving the osseointegration of the cranial implant (see Fig. 3C) [42].

The SPS process is a modern consolidation technique in the powder metallurgy field with simultaneous imposed low voltage and high pulse current to uniaxial pressure-assisted hydraulic punches/electrodes [43]. In this process, a high densification level can be obtained in a short time and a wide range of sintering temperature (up to 2000 °C) with the fast heating rate (up to 1000 °C/min) compared to the conventional powder metallurgy methods such as hot isostatic pressing (HIP). The electrical DC pulsed in a vacuum chamber generates the spark discharge, passing through graphite mold (with different diameters) and powder particles (metals, ceramics, or cermets) by thermocouple or pyrometer controlling [44]. The spark plasma sintering device (SPS, supplied by *FCT Systeme GmbH*, [45]) surrounded by a vacuum chamber and a glovebox with nitrogen flow inside to avoid oxygen contamination was used in our process. Three hybrid metal-ceramic samples sintered with identical SPS parameters, 20 MPa pressure, 1000 °C temperature, 100 °C/min ramp rate and 15 min dwell time are shown in Fig. 4. Top. The increase in pressure (from 3 MPa to 20 MPa) and temperature (from 300 °C to 1000 °C) is achieved inside a 20 mm graphite die/mold (Fig. 4. Bottom). Post-processing for lattice structures (not solid/bulk) can include polishing (1. Outermost struts after printing by SLM process, 2. Bottom and top after filing by SPS), blasting by Al_2O_3 nanoparticles (for sticked/unmelted particles to inner struts), nitriding (keeping in the vacuum furnace under flowing of Ni to have TiN struts) and coating (chrome plating via chemical vapor deposition), etc. that is not applied here.

2.3. Impact test

The *ball-on-plate* impact test we designed was used to test the fabricated cylindrical samples (20 mm diameter and 6–8 mm height, comprising hybrid cermets or metal alloys), see Fig. 5, [46,47]. The sample
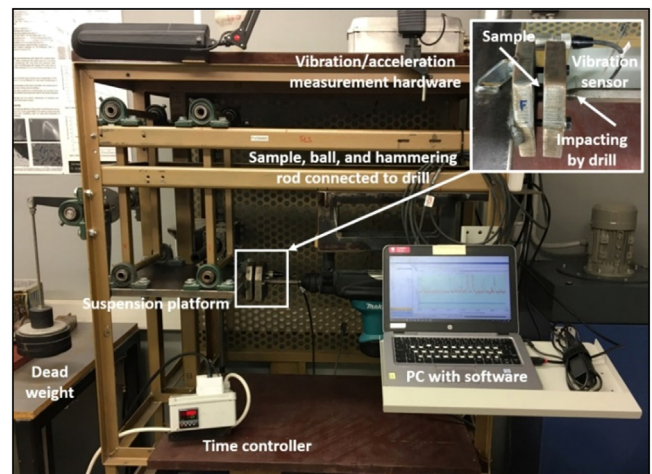
is fixed on the platform and receives multiple impacts through 1.0 cm diameter ZrO_2 ball (95% ZrO_2 stabilized by 5% Y_2O_3, supplied by *Tosoh Corp.*). More precisely, 30 impacts were induced by a hammering drill, supplied by *Makita*, with an energy of 5.6 J and a frequency of 27.5 Hz, a compressive force 98.1 N (equivalent to 10 kg), and a hammering duration of 1.1 s. The design of hammer drill, the arrangement of the specimen and ball, the pendulum-type suspension platform connected to the vibration sensor and an adjustable dead weight are shown in Fig. 5. Impact acceleration during multiple impact was measured using a *PCH 1420* accelerometer, attached to the platform.

2.4. Finite element analysis

Prediction of deformation and stress, via e.g. finite element analysis (FEA), can be very useful before prototyping. In this study, the potential of using TiNi or Ti22Al25Nb together with Ti6Al4V is also evaluated using FEA for cranial implants. In this case, *Ansys Workbench* and *AUTODYN Solver* (structural explicit dynamic module) are used to analyze the response of the scaffold to loading. The same geometry, i.e. disks with 20 mm in diameter and 16 mm in height, was chosen for the fabricated samples. The Young modulus and Poisson's ratios are 110 GPa and 0.31 for Ti6Al4V, 70 GPa and 0.33 for TiNi, and 90 GPa and 0.32 for Ti22Al25Nb. Among them, TiNi has a lower Young modulus (better malleability) and higher Poisson's ratio (due to superelasticity) compared to the other two Ti-alloys.

3. Results and discussion

3.1. Metallic scaffold (lattice structure)

Fig. 6 shows the SEM micrograph of the Ti6Al4V scaffold with 2.0 mm cell size, 0.5 mm strut diameter, and 50 μm layer thickness used in this study (see Fig. 6). Three important aspects related to the fabrication of metal-ceramic composites should be mentioned:

1 Post-processing (polishing, blasting, coating, etc.) is necessary for characterization after printing and/or sintering [48,49]. Depending on the size/architecture of the lattice unit cells (in our case, four-struts cross-sectional diamond-type), the appearance of the cross-section is position-dependent and the shape may be distorted due to shrinkage during sintering and partial removal during polishing [50]. In this case, both the "top" and "bottom" faces are considered at generic (reference) locations in the structure (Fig 6A). Depending
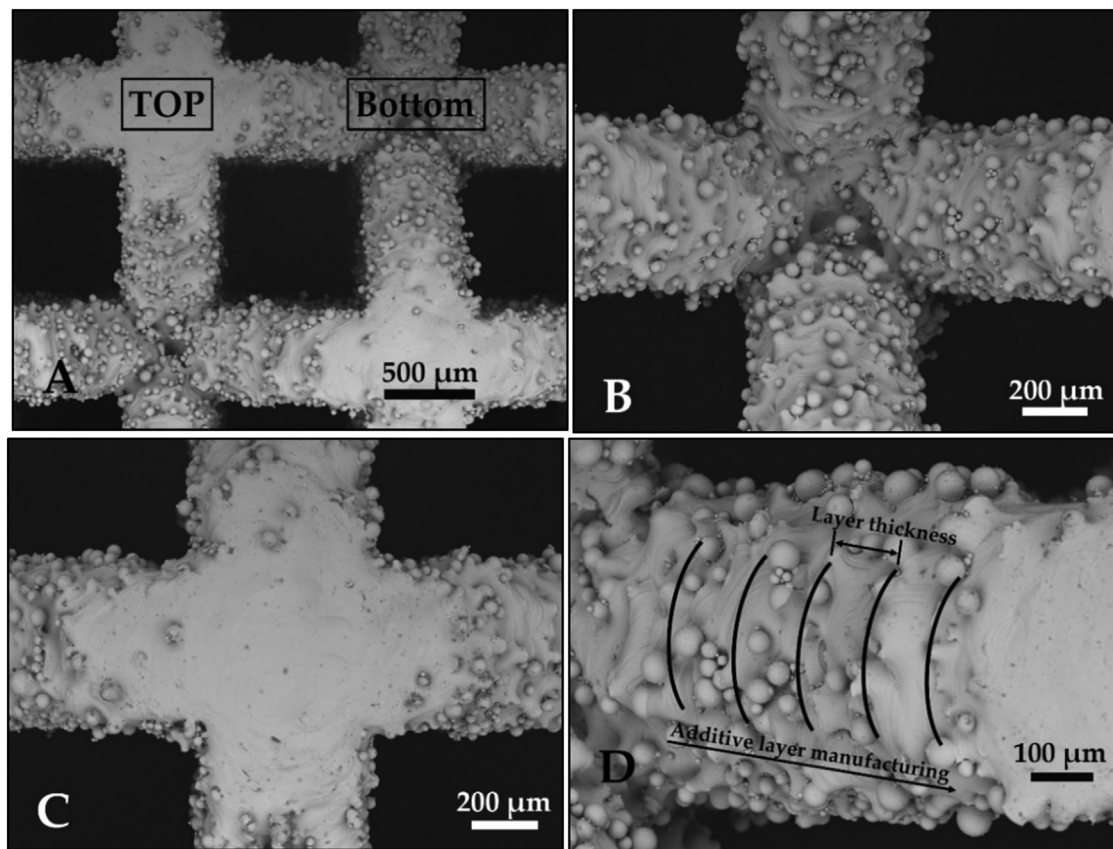
Fig. 6. SEM micrograph of a Ti6Al4V lattice with 2.0 mm cell size, 0.5 mm strut diameter and ≈ 40% volume fraction: A) Subsection of the mesh structure with top and bottom views, B) and C) Unit cell of the body-centered cubic (BCC) lattice configuration with four cross-sectional struts (bottom and top, respectively), and D) Perspective view of the strut fabricated with 50 μm layer thickness.

on the operational pressure-temperature relation in SPS and ceramic-metal specifications (proportion of metal and ceramic powder, size and shape, melting points, etc.), about 20–40% reduction of the sample height might occur.

2 Bulk/plain structures built with 25 μm layer thickness (mostly available in smaller/laboratory size 3D printers like the *Realizer SLM®50* device) [51,52] demonstrate higher fracture strength than those built by 50 μm layer thickness (achievable with devices for larger/industrial-size samples, like the *Realizer SLM®280*) [53]. Nevertheless, the 50 μm layer thickness method provides sufficient strut strength compared to human bones applied for craniofacial defects and tissue engineering (Fig. 6D).

3 We used vibrational technique to simplify filling of the spaces (allocating ceramic powders into the grid metal struts), because biomaterial powders like wollastonite or hydroxyapatite have irregular shape (see Fig. 3), but for other antibacterial powders like ZrO_2 and TiO_2 with spherical shapes there is no need to apply this technique.

A combined SLM-SPS procedure was developed for biomaterials, metamaterials, virucidal and tribological applications. The original idea [52] that has targeted the refractory materials (specially TBM device, [51]), has metallic part at the bottom, functionally graded hard material (ceramics or coated diamond particles) in inner layers (which are embedded in 3D-printed lattice and sintered together) and pure ceramic at the top for higher abrasion resistance. Regarding the application, we can change many different parameters: mainly strut diameter and cell size of the lattice/grid, which define the proportion of ceramic and metal. In the current work, bulk top/bottom parts are neglected and metal/ceramic have uniform proportions.

3.2. FEA of metallic lattice structures

The von Mises stress distribution and deformation/displacement under compression of Ti-based alloys using FEA (*SolidWorks* CAD model and *Ansys* simulation) are shown in Fig. 7A-7F. Similar to the experimental lattices, the diameter of the simulated lattice structures is 20 mm and height is 16 mm. The smooth change from one color to another in the contours shows the ductility of TiNi due to the high nickel content (see Figs. 7C and 7D). Whereas, the predominant dark-blue colors in the stress distribution of Fig. 7E show more stiffness of Ti22Al25Nb under compression (the structure has not reached the plastic region). It is shown in Fig. 7F, that the deformation is minimal, which means higher compression strength for Ti22Al25Nb. The comparison of Figs. 7B and 7D shows that the contours (ranging from blue to red) are lighter for Ti6Al4V and darker for softer material like TiNi. This FEA shows that Ti6Al4V, TiNi, and Ti22Al25Nb have a negligible difference in mechanical response when subjected to a compression test. Consequently, depending on the application (superelasticity, conductivity, ductility, malleability, lightness, architecture, etc.), they are all quite interchangeable for the lattice structure.

Metallic scaffolds will solely bear the load and impact since ceramic powders will be lixiviated to the real-time body fluids. Ceramic powders in the metal-ceramic composite will lead to bio-mineralization. Eventually, these ceramic elements can interact with the body fluids to induce bone formation even in the *Dura* mater (connective tissue surrounds the brain) and the defected area. Considering the real-time scenario or *in-vivo* conditions, metallic scaffolds will solely bear the load and ceramic powders will be released or lixiviated to the fluids since ceramic elements used in this study are osteoconductive. This is the reason that only
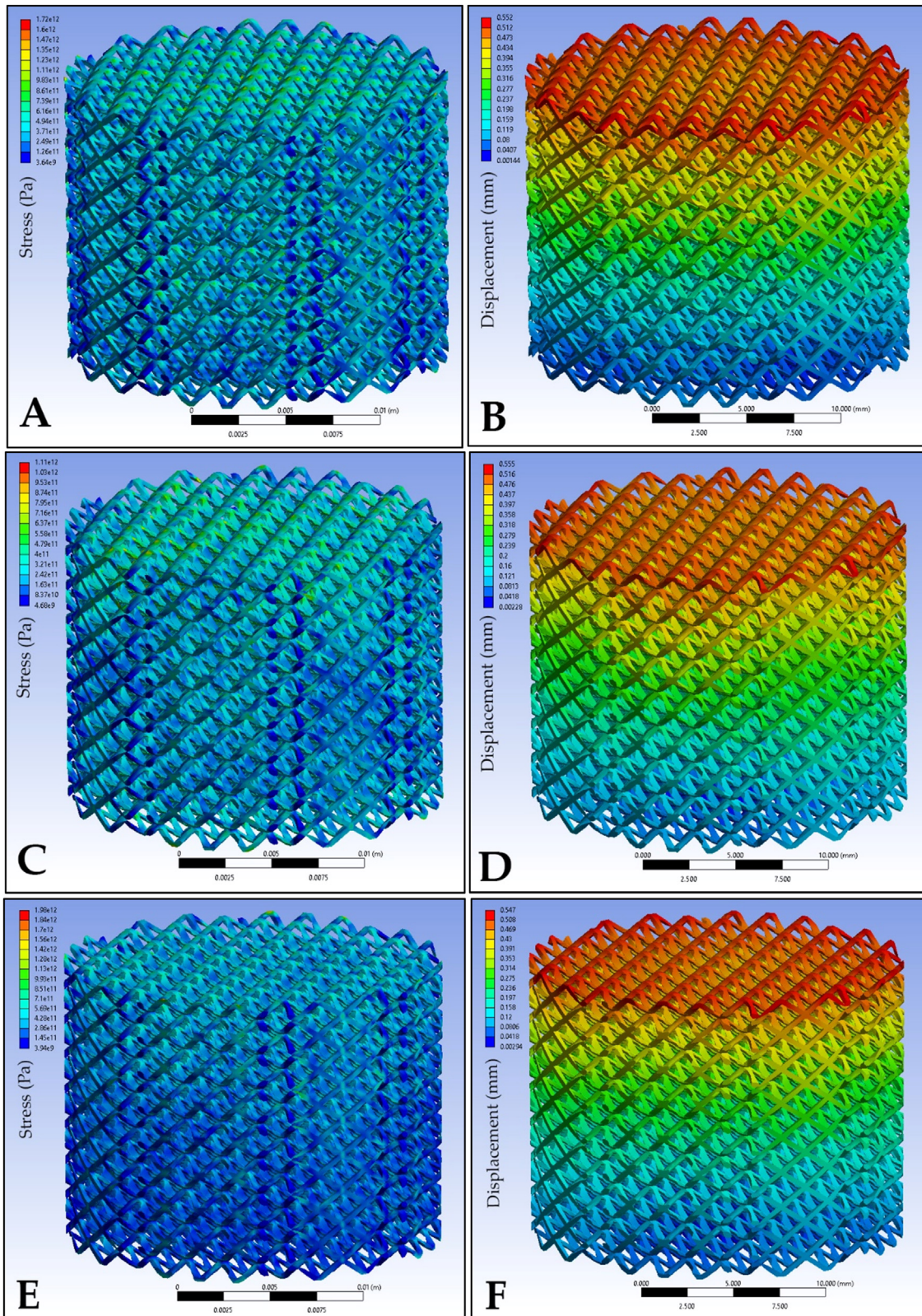
Fig. 7. Finite element analysis (FEA) of titanium alloys: A) Stress distribution of Ti6Al4V, B) Displacement of Ti6Al4V, C) Stress distribution of TiNi, D) Displacement of TiNi, E) Stress distribution of Ti22Al25Nb, F) Displacement of Ti22Al25Nb. The diameter of all lattice structures is 20 mm and the height is 16 mm (the same as tested samples).
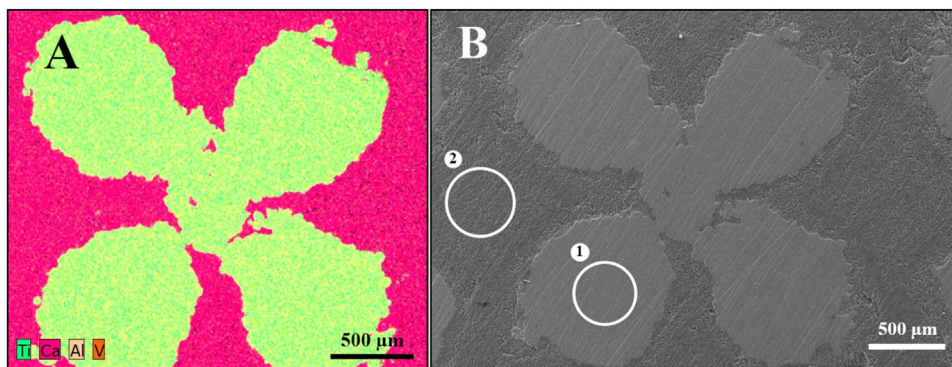
Fig. 8. EDS mapping of the main elements for the Ti6Al4V-CaSiO₃ sample: A) Color map, B) Image indicating the position of the zones. Average distribution in the metallic zone (zone 1: Titanium 90.99%, Aluminum 5.42%, and Vanadium 2.35%) and the ceramic zone (zone 2: Oxygen 39.17%, Calcium 32.30% and Silicon 18.50%).

lattice structure (without filled ceramic) is applied for compression test here. In this FEA, 1 mm displacement of punch is applied in 0.01 s; therefore, this compression is similar to a high-energy impact. Very fast compressing causes a maximum of 0.552, 0.555, and 0.547 mm plastic deformation for Ti6Al4V, TiNi and Ti22Al25Nb, respectively. The difference is negligible (due to the ductility of TiNi and rigidity of Ti22Al25Nb). On the other hand, the average Von-Mises stress in structures is $\approx$ 600 MPa for Ti6Al4V, $\approx$ 550 MPa for TiNi, and $\approx$ 400 MPa Ti22Al25Nb.

3.3. Metal-ceramic composite

The uniform distribution of the powders plays a crucial role in the mechanical response (mainly influenced by the metallic structure during the SLM process) or bioactivity (mainly influenced by the ceramic consolidation during the SPS). Energy dispersive spectroscopy (EDS) mapping of the Ti6Al4V-CaSiO₃ sample is shown in Fig. 8 for both the ceramic and metal-rich zones. Ti6Al4V struts with 0.5 mm diameter and $\approx$ 40% volume fraction overspreads due to SPS pressure (zone 1), whereas, CaSiO₃ with $\approx$ 60% volume fraction of composite embeds inside struts and consolidate (zone 2).

Figs. 9A-9F show the microstructure and boundary region of the metallic struts and the binder ceramic (obtained by scanning electron microscopy, *Hitachi TM-1000* tabletop, SEM) for W, W-Si, and W62, respectively. During the increasing temperature in the SPS process, the shape of the struts' cross-sections may change slightly from circular to oval (Fig. 9A), even though the sintering process is performed at low-pressure condition (20 MPa). This phenomenon is due to the lower sintering temperature and higher molecular motion of the metal (Ti-based) compared to the ceramic (W-based). The sintering process and densification are successfully carried out in all three samples. W (wollastonite) consistently maintains its porous structure (Fig. 9B), while W-Si exhibits some minor cracks around the struts (Fig. 9D). Moving away from the boundary with the metal struts, the roughness decreases and the ceramic zone is more condensed (Fig. 9E). W62 is a bioactive glass-ceramic that has the smoothest surface after polishing (Fig. 10B). Note that it is possible to significantly reduce the porosity (especially at the boundary) by increasing the SPS pressure, but for the *in-vivo* applications, the higher porosity may be beneficial. The porosity level of the ceramic-metal interphase region decreases and the degree of densification increases from W to W-Si and W-Si to W62. Since the metallic scaffolds are bearing the mechanical loads (in compression and impact) and holding the composite structure together, deliberately induced cracks or pores in the ceramic region can be used for drug delivery, without significantly reducing the strength of the implant.

3.4. Impact test results

The SEM micrograph (Fig. 10A) of the Ti6Al4V-CaSiO₃ hybrid metal-ceramic deformed by multiple dynamic impacts shows an effect zone with 2880 μm in diameter. In Figs. 10B and 10C, cracks can be seen across the metal strut and a separation at the metal-ceramic interface, respectively. The higher value of the platform acceleration during the impact on the y-axis in Fig. 10D illustrates the higher stiffness (lower damping of the impact energy) of the sample against the ball/drill impact, the higher strength and the lower deformation and penetration. However, the diameter of the deformed zone is 2880 μm, but because of the impact damping by the metal struts, the penetrated volume is only approximately 0.6 mm³, which means that the penetration depth is quite small. The application of the presented wear/impact system can also be used (if required) to produce local damage and pores in such a hybrid metal-ceramic biomaterial for local adjustment of the drug delivery rate.

The stiffness and strength of Ti22Al25Nb and shape-memory/superelasticity of TiNi have highlighted them as useful replacements for the popular Ti6Al4V scaffolds, especially for our craniofacial application exposed to impact. The optimized SPS parameters for the bulk (solid, without the addition of ceramics) Ti-based Ti6Al4V, TiNi, and Ti22Al25Nb samples were as follows: 50 MPa pressure, 1000 °C temperature, 100 °C /min heating rate (ramp) and 5 min holding (dwell) time. These metallic titanium-balanced samples also had 20 mm in diameter and approximately 6–8 mm in height. The result of the multiple impact test for bulk Ti6Al4V, TiNi, and Ti22Al25Nb samples is shown in Fig. 11. The diameter and affected/lost/indented volume of penetration for bulk titanium alloys are 2506 μm and 1.1 mm³ for Ti6Al4V, 2912 μm and 1.8 mm³ for TiNi, and 2410 μm and 0.9 mm³ for Ti22Al25Nb, respectively. As expected (according to FEA), Ti22Al25Nb shows the best performance against the impact in the experiments. It can be observed that after the initial impacts, the acceleration amplitude goes down for Ti22Al25Nb. This can be interpreted as a change in the damping capacity. For Ti alloys, we can observe from Fig. 6a correlation between the analytical result of the compression test of the scaffolds and the experimental result of impact tests on the solid disks in Fig. 11. Accordingly, the deformation of the structures in Figs. 7B, 7D, and 7F correspond to the indent diameter in Figs. 11A, 11B, and 11C, respectively. Impact test outputs from Figs. 10 and 11 demonstrate a higher diameter of the deformed zone and a higher average of acceleration peaks, and a lower indent volume for metal-ceramic composite (CaSiO₃-Ti6Al4V) in comparison with bulk metal (Ti6Al4V).

Positive maximum vibration peaks of each of the 30 impacts were derived from acceleration curves of Ti alloys and shown in Fig. 12A. Low-intensity impacts before and after the full-load hammering (less than 200 m/s²) are neglected. The average of these peaks for Ti6Al4V, TiNi, and Ti22Al25Nb samples are approximately 960, 530, and 780 m/s², respectively. The straightness of the TiNi curve (compared to the fluctuation of Ti6Al4V in the first peaks and regressive in the rest) shows stable damping of the impact. The proximity to the hypothetical diagonal line (gray line) shows that the material applies more impact energy dur-
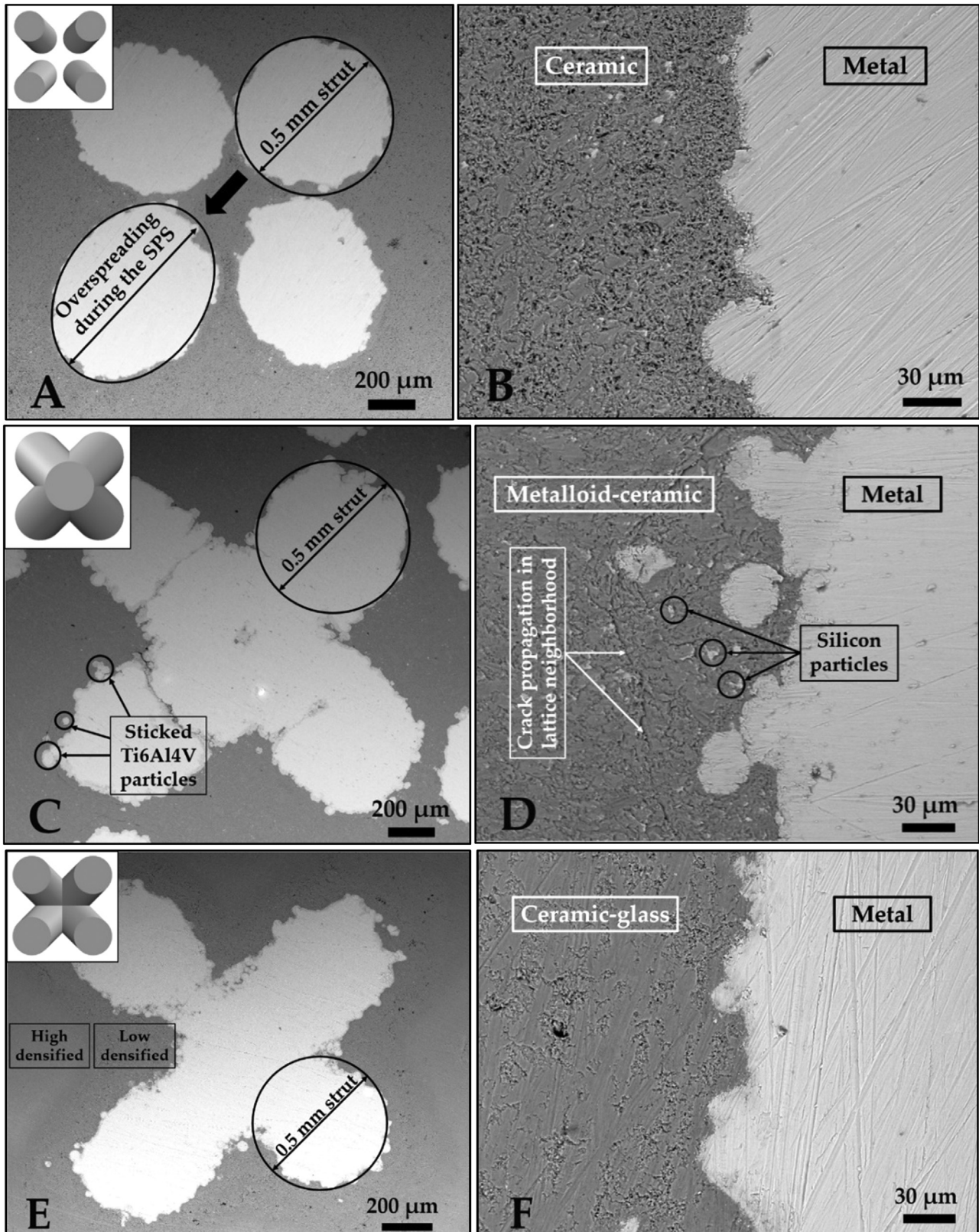
Fig. 9. SEM images of A) Metallic Ti6Al4V unit cell embedded in consolidated ceramic W, B) Boundary region of Ti6Al4V-W biomaterial ceramic, C) Metallic Ti6Al4V unit cell embedded in consolidated ceramic W-Si, D) Boundary region of Ti6Al4V-(W-Si) biomaterial metalloid-ceramic, E) Metallic Ti6Al4V unit cell embedded in consolidated ceramic W62, and F) Boundary region of Ti6Al4V-W62 biomaterial ceramic-glass.
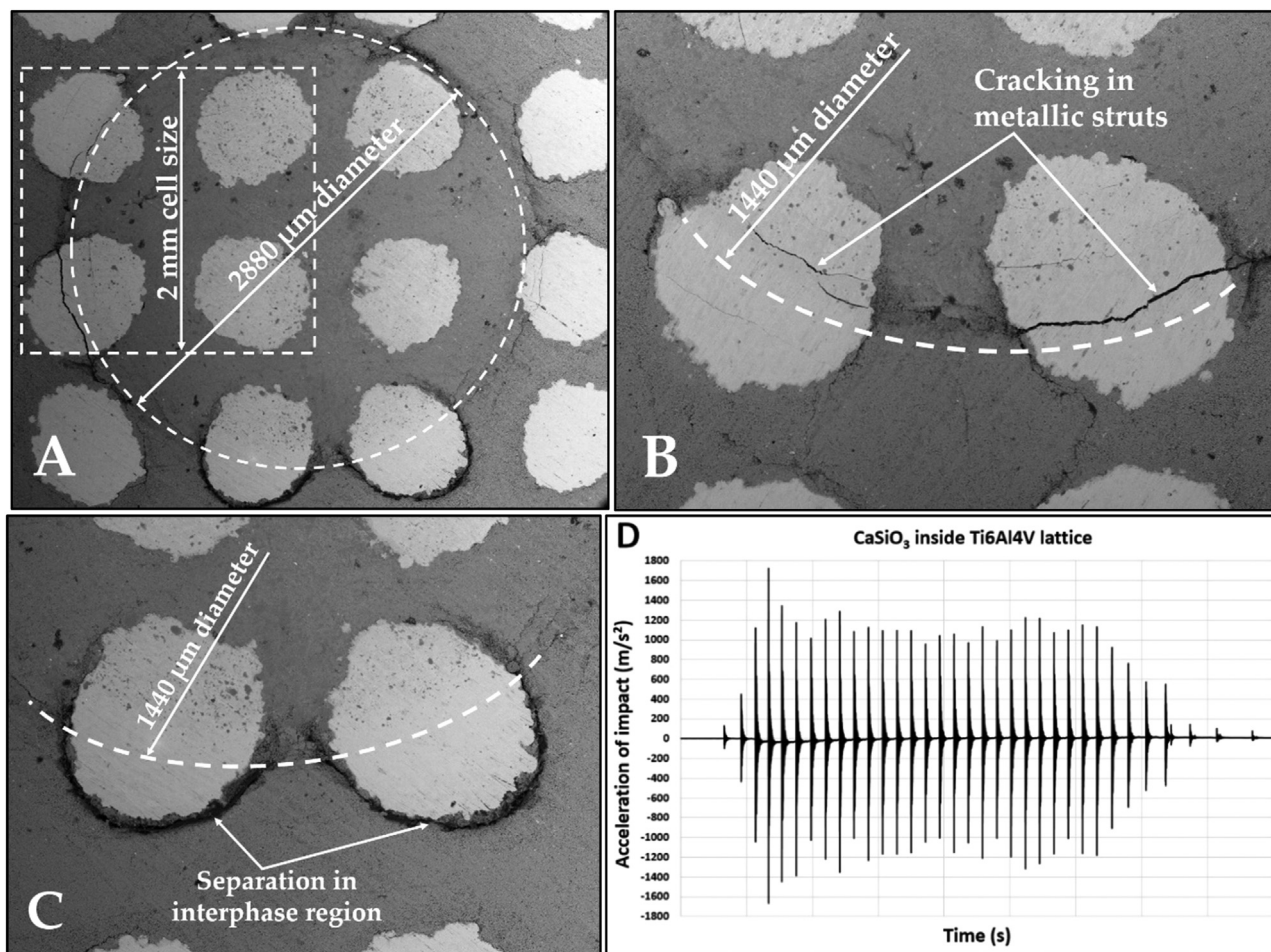
Fig. 10. SEM micrograph of a zone affected by multiple dynamic impacts: A) CaSiO$_3$ ceramic within a Ti6Al4V metallic lattice with a cell size of 2 mm, B) Cracks in the struts, C) Detachment in the metal-ceramic interphase region, and D) Acceleration diagram for 30 impacts. The diameter of the deformed region is approximately 2880 μm, the penetrated volume is approximately 0.6 mm^3, and the average of acceleration peaks is approximately 1090 m/s^2.

ing plastic deformation without failure (see Fig. 12B). Based on the test results in this study, one can conclude that TiNi provides the best and most stable damping of the impact, while this is realized at the expense of the plastic deformation (volume of the imprint). On the other hand, Ti6Al4V with the lowest plastic deformation exhibits correspondingly the lowest damping of the impacts. Ti22Al25Nb provides the average damping with the smallest volume of the indent, which suggests that the damping is realized not only by plastic deformation but also to a large extent by elastic deformation.

3.5. State-of-art of hybrid composite design

The current study stands for the design of craniofacial or possible maxillofacial implants through combined additive manufacturing and powder metallurgy. Fast prototyping based on SLM [54] and SPS techniques provides biomedical/antibacterial properties with proper mechanical properties. This concept design is depicted in Fig. 13 for artificial bone replacement. Wollastonite- and hydroxyapatite-based powders have great potential to fill inside titanium alloys with complex lattice structures in different organisms. Definition of triple parameters for SLM (laser power, scan speed, and layer thickness) and SPS (time, pressure, temperature) have crucial roles in this development. Post-processing procedures may be a simple step like polishing/blasting/coating, or complicated as subtractive manufacturing or graphite mold design for forming the final product. The implants can be the potential solutions

for the temporal lobe implants for osteosynthesis in the cranium by supporting the bone fractures [55]. These metal-matrix composites (MMCs, Ti6Al4V reinforced with CaSiO$_3$) concerning the mechanical anchorage are of extreme prime importance or relevance where the optimal transference of strength and stiffness is required between the reinforcing material (ceramics) and metal matrix for cranium bone fractures. The implementation of the SPS allowed closed interfacial contact between metal and ceramic component therefore allowing excellent stress transference, which is beneficial for the temporal lobe implants for cranium bones fixation. Following outcomes of this work, authors investigate "thermal conductivity for in-vivo Ti-based (e.g. the present work) and electrical conductivity in-vitro Cu-based (e.g. [56,57])". This work will similar methodology and compare experimental/numerical results as well.

We would like to highlight the following two messages in this work:

I Ti6Al4V-CaSiO$_3$ hybrid metal-ceramic biomaterial could be used for fabrication of medical implants, e.g. as a craniofacial plate that is resistant to multiple dynamic impacts, collision with heavy objects, etc.

II Counterintuitively, by deliberately inducing cracks in the bioceramic and bio-TPMS composites to deliver drugs (e.g. antibiotic vancomycin, oxygen transport, or fluid permeability) during healing. Due to the proposed architecture that promotes both strength and hardness of the material, the implant would still be effective.
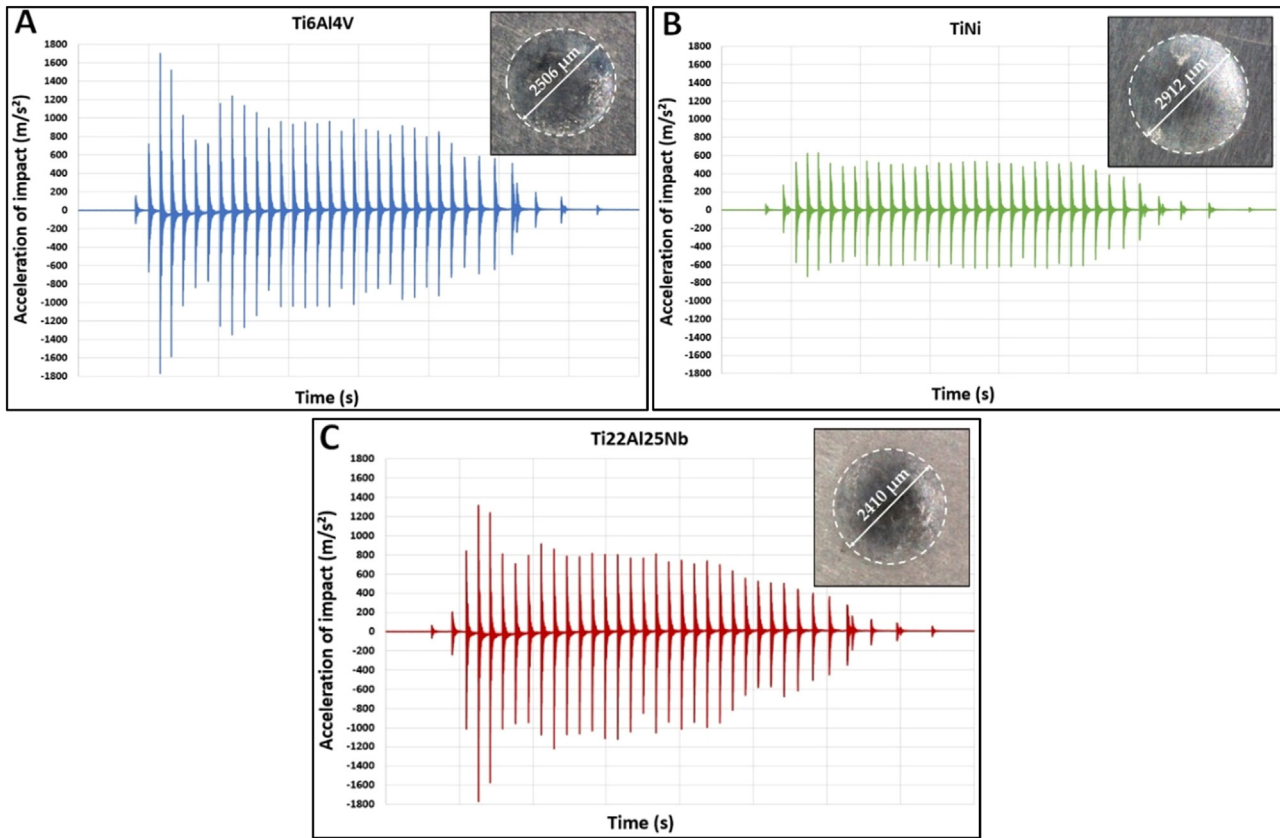
Fig. 11. Acceleration diagrams for approximately 30 impacts: A) Ti6Al4V formed a 2506 μm diameter and an indented volume of approx. 1.1 mm³, B) TiNi formed a 2912 μm diameter and an indent volume of approximately 1.8 mm³, and C) Ti22Al25Nb formed a 2410 μm diameter and an indent volume approximately 0.9 mm³.
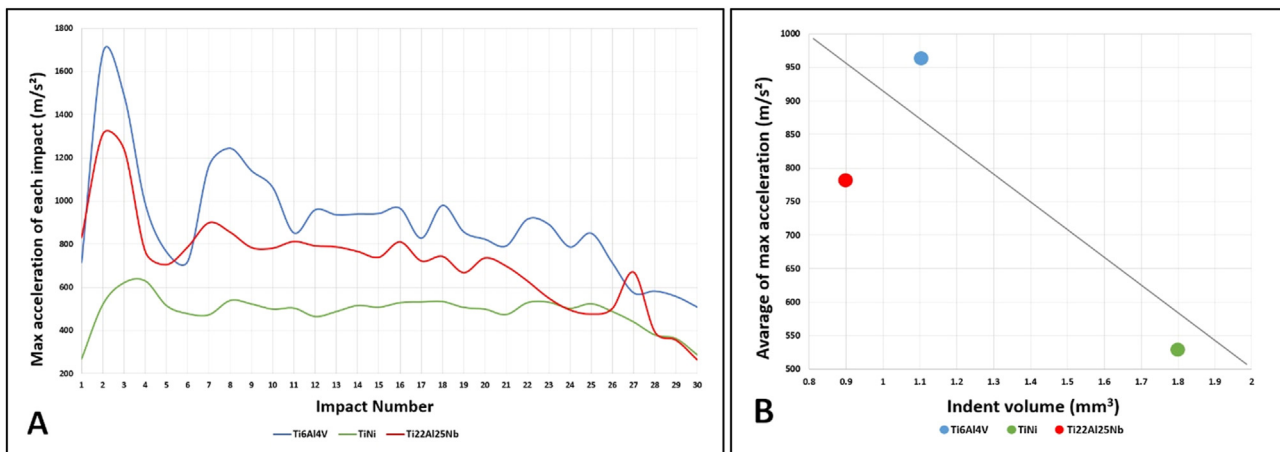

Fig. 12. Diagrams of A) Positive maximum acceleration/vibration peaks/values of each impact (from Fig. 11), B) Dynamic hardness versus volume of the indent (ductility-rigidity graph).

4. Conclusion

In this paper, the fabrication procedure of hybrid metal-ceramic bio-material by the combined approach of additive manufacturing (selective laser melting, SLM process) and powder metallurgy (spark plasma sintering, SPS) is presented. We show that Ti6Al4V lightweight metallic scaffolds filled with $CaSiO_3$-based bioceramics have a good *in-situ* bonding during SPS, which is required for the potential craniofacial implants. Wollastonite-based bioceramic powders containing $CaSiO_3$ (100% wollastonite), Si-$CaSiO_3$ (50 wt.% wollastonite), and $CaSiO_3$_$Ca_3(PO_4)_2$_$MgCa(SiO_3)_2$ (62 wt.% wollastonite ceramic glass) can be embedded in vacant spaces of the Ti6Al4V scaffold by SPS. Metallic lattice solely bears the load and impact since embedded bioceramic will be lixiviated to the real-time body fluids. Experimental re-
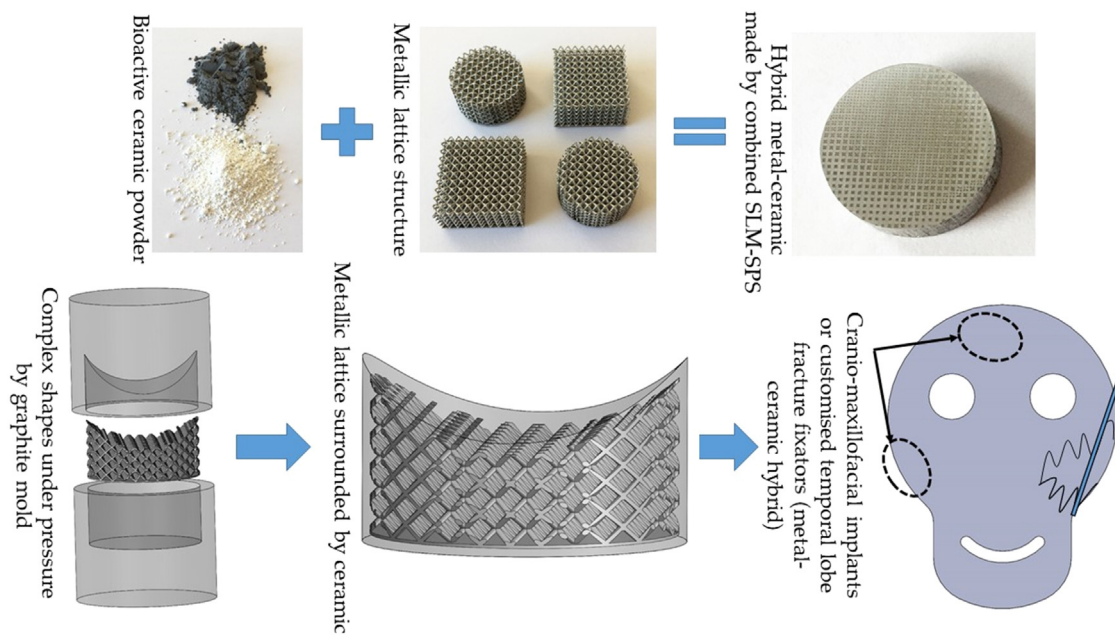
Fig. 13. Concept design for cranio-maxillofacial implant. Powders like wollastonite, hydroxyapatite, and derivatives of these substances in nanoscale have the potential to fill inside titanium alloys with arbitrary lattice structures. This strut-based lattice or surface-based scaffolds can be fabricated in a short time by selective laser melting method, sintered with ceramic in spark plasma sintering, and provide the hybrid bio-metal-ceramic composite. Development of this method requires the investigation of curvature for complex shapes, densification in surface, morphology under loading, and bioactivity measurement for in-vivo application.

sults show limited cracking in the impact region of the silicon doped wollastonite ceramic (W-Si) and the metallic struts interface when subjected to multiple dynamic impacts. A higher degree of porosity of wollastonite (W) is changed to a higher densification level in wollastonite ceramic glass (W62) in the ceramic zone of cermet composite. The volume and depth of indentation were small (approximately 0.6 mm^3 for CaSiO$_3$-Ti6Al4V composite and approximately 1.1 mm^3 for solid Ti6Al4V). Ti6Al4V, TiNi, and Ti22Al25Nb alloys were also sintered by SPS and tested under the impact wear test. The results of FEA (*SolidWorks* and *Ansys* couple software) for high single impact load (compression/displacement by punches) applied over a short period of time showed a similar rating of the materials. It was found that TiNi provides the best damping (proper for craniofacial implant) of the impacts, while in the case of Ti22Al25Nb the damping included a higher portion of elastic deformation. Another important result of the proposed fabrication process implies that since the metallic scaffolds can both, bear the mechanical loads and holding the composite structure together, deliberately induced cracks or pores in the ceramic region can be exploited for drug delivery without significantly reducing the strength of the implant. Future work may investigate the "gradient curved cranio-maxillofacial skull part" applications. The curved parts can be designed with the denser metallic layer in the outermost layers and the volume fraction of the lattice structure can be functionally degraded towards the innermost layers for filling by bioactive hydroxyapatite/wollastonite ceramic.

Declaration of Competing Interest

The authors, Ramin Rahmani, Nikhil Kamboj, Maksim Antonov, Miha Brojan and Konda Gokuldoss Prashanth, declare that there are no conflicts of interest regarding the article entitled "*Hybrid metal-ceramic biomaterials fabricated through powder bed fusion and powder metallurgy for improved impact resistance of craniofacial implants*" in "*Journal of Materialia*". The manuscript is original and has not been published in other journals or conferences.

CRediT authorship contribution statement

Ramin Rahmani: Conceptualization, Methodology, Investigation, Writing – original draft. **Nikhil Kamboj:** Conceptualization, Investigation. **Miha Brojan:** Methodology, Supervision, Funding acquisition. **Maksim Antonov:** Methodology, Writing – review & editing. **Konda Gokuldoss Prashanth:** Writing – review & editing, Funding acquisition.

Acknowledgments

References

[1] G.L. Koons, M. Diba, A.G. Mikos, Materials design for bone-tissue engineering, Nat. Rev. Mater. 5 (2020) 584–603.

[2] U.G. Wegst, H. Bai, E. Saiz, A.P. Tomsia, R.O. Ritchie, Bioinspired structural materials, Nat. Mater. 14 (2015) 23–36.

[3] J. McKittrick, P.Y. Chen, L. Tombolato, E.E. Novitskaya, M.W. Trim, G.A. Hirata, E.A. Olevsky, M.F. Horstemeyer, M.A. Meyers, Energy absorbent natural materials and bioinspired design strategies: a review, Mater. Sci. Eng. C 30 (2010) 331–342.

[4] S. Signetti, N.M. Pugno, Evidence of optimal interfaces in bio-inspired ceramic–composite panels for superior ballistic protection, J. Eur. Ceram. Soc. 34 (2014) 2823–2831.

[5] S.M. Ahmadi, R. Hedayati, Y. Li, K. Lietaert, N. Tümer, A. Fatemi, C.D. Rans, B. Pouran, H. Weinans, A.A. Zadpoor, Fatigue performance of additively manufactured meta-biomaterials: the effects of topology and material type, Acta Biomater. 65 (2018) 292–304.

[6] F.S.L. Bobbert, K. Lietaert, A.A. Eftekhari, B. Pouran, S.M. Ahmadi, H. Weinans, A.A. Zadpoor, Additively manufactured metallic porous biomaterials based on minimal surfaces: a unique combination of topological, mechanical, and mass transport properties, Acta Biomater. 53 (2017) 572–584.

[7] K. Tai, M. Dao, S. Suresh, A. Palazoglu, C. Ortiz, Nanoscale heterogeneity promotes energy dissipation in bone, Nat. Mater. 6 (2007) 454–462.

[8] R. Wang, H.S. Gupta, Deformation and fracture mechanisms of bone and nacre, Annu. Rev. Mater. Res. 41 (2011) 41–73.

[9] J. Sun, B. Bhushan, Hierarchical structure and mechanical properties of nacre: a review, RSC Adv. 2 (2012) 7617–7632.

[10] G.X. Gu, M. Takaffoli, A.J. Hsieh, M.J. Buehler, Biomimetic additive manufactured polymer composites for improved impact resistance, Extreme Mech. Lett. 9 (2016) 317–323.

[11] A.A. Zadpoor, Meta-biomaterials, Biomater. Sci. 8 (2020) 18–38.

[12] S. Chen, Y. Shi, Y. Luo, J. Ma, Layer-by-layer coated porous 3D printed hydroxyapatite composite scaffolds for controlled drug delivery, Colloids Surf. B 179 (2019) 121–127.

[13] Y. Dong, X. Sun, Z. Zhang, Y. Liu, L. Zhang, X. Zhang, Y. Huang, Y. Zhao, C. Qi, A.C. Midgley, S. Wang, Regional and sustained dual-release of growth factors from biomimetic tri-layered scaffolds for the repair of large-scale osteochondral defects, Appl. Mater. Today 19 (2020) 100548.

[14] T. Zandrini, O. Shan, V. Parodi, G. Cerullo, M.T. Raimondi, R. Osellame, Multi-foci laser microfabrication of 3D polymeric scaffolds for stem cell expansion in regenerative medicine, Sci. Rep. 9 (2019) 1–9.

[15] D. Lindner, K. Schlothofer-Schumann, B.C. Kern, O. Marx, A. Müns, J. Meixensberger, Cranioplasty using custom-made hydroxyapatite versus titanium: a randomized clinical trial, J. Neurosurg. 126 (2017) 175–183.

[16] L.K.B. Linder, U. Birgersson, K. Lundgren, C. Illies, T. Engstrand, Patient-specific titanium-reinforced calcium phosphate implant for the repair and healing of complex cranial defects, World Neurosurg. 22 (2019) 399–407.

[17] J. Sundblom, D. Nowinski, O. Casar-Borota, M. Ryttlefors, Removal of giant intraosseous meningioma followed by cranioplasty using a custom-made bioceramic implant: case report, J. Neurosurg. (2018) 1–5.

[18] S. Berretta, K. Evans, O. Ghita, Additive manufacture of PEEK cranial implants: manufacturing considerations versus accuracy and mechanical performance, Mater. Des. 139 (2018) 141–152.

[19] F.El. Halabi, J.F. Rodriguez, L. Rebolledo, E. Hurtós, M. Doblaré, Mechanical characterization and numerical simulation of polyether-ether-ketone (PEEK) cranial implants, J. Mech. Behav. Biomed. Mater. 4 (2011) 1819–1832.

[20] G. Ambrogio, G. Palumbo, E. Sgambitterra, P. Guglielmi, A. Piccininni, L. De Napoli, T. Villa, G. Fragomeni, Experimental investigation of the mechanical performances of titanium cranial prostheses manufactured by super plastic forming and single–point incremental forming, Int. J. Adv. Manuf. Technol. 98 (2018) 1489–1503.

[21] D.B. Matic, P.N. Manson, Biomechanical Analysis of Hydroxyapatite Cement Cranioplasty, J. Craniofac. Surg. 15 (2004) 415–422.

[22] S. Lewin, J. Åberg, D. Neuhaus, H. Engqvist, S.J. Ferguson, C. Öhman-Mägi, B. Helgason, C. Persson, Mechanical behaviour of composite calcium phosphate-titanium cranial implants: effects of loading rate and design, J. Mech. Behav. Biomed. Mater. 104 (2020) 103701.

[23] S. Liu, Y.C. Shin, Additive manufacturing of Ti6Al4V alloy: a review, Mater. Des. 164 (2019) 107552.

[24] E. Louvis, P. Fox, C.J. Sutcliffe, Selective laser melting of aluminium components, J. Mater. Process. Technol. 211 (2011) 275–284.

[25] Q. Jia, D. Gu, Selective laser melting additive manufacturing of Inconel 718 superalloy parts: densification, microstructure and properties, J. Alloys Compd. 585 (2014) 713–721.

[26] S.L. Sing, W.Y. Yeong, F.E. Wiria, Selective laser melting of titanium alloy with 50wt.% tantalum: microstructure and mechanical properties, J. Alloys Comp. 660 (2016) 460–471.

[27] Densification and properties of transition metal borides-based cermets via spark plasma sintering, J. Eur. Ceram. Soc. 26 (2006) 2431–2440.

[28] O. Guillon, J. Gonzalez-Julian, B. Dargatz, T. Kessel, G. Schierning, J. Räthel, M. Herrmann, Field-Assisted Sintering Technology/Spark Plasma Sintering: mechanisms, Materials, and Technology Developments, Adv. Eng. M 16 (2014) 830–849.

[29] R. Rahmani, M. Antonov, N. Kamboj, Modelling of impact-abrasive wear of ceramic, metallic, and composite materials, Proc. Est. Acad. Sci. 68 (2019) 191–197.

[30] R. Rahmani, M. Rosenberg, A. Ivask, L. Kollo, Comparison of mechanical and antibacterial properties of TiO_2/Ag ceramics and $Ti6Al4V-TiO_2/Ag$ composite materials using combining SLM-SPS techniques, Metals (Basel) 9 (2019) 874.

[31] https://www.slm-solutions.com/products-and-solutions/powders (accessed on 20 April 2021).

[32] https://www.tls-technik.de/en/products.html (accessed on 20 April 2021).

[33] https://en.c-semt.com/metal-powder (accessed on 20 April 2021).

[34] E. Sallica-Leva, A.L. Jardini, J.B. Fogagnolo, Microstructure and mechanical behavior of porous Ti-6Al-4V parts obtained by selective laser melting, J. Mech. Behav. Biomed. Mater. 26 (2013) 98–108.

[35] S. Saedi, N.S. Moghaddam, A. Amerinatanzi, M. Elahinia, H.E. Karaca, On the effects of selective laser melting process parameters on microstructure and thermomechanical response of Ni-rich NiTi, Acta Mater. 144 (2018) 552–560.

[36] Y.X. Wang, K.F. Zhang, B.Y. Li, Microstructure and high temperature tensile properties of Ti22Al25Nb alloy prepared by reactive sintering with element powders, Mater. Sci. Eng.: A 608 (2014) 229–233.

[37] N. Kamboj, M.A. Rodríguez, R. Rahmani, K.G. Prashanth, I. Hussainova, Bioceramic scaffolds by additive manufacturing for controlled delivery of the antibiotic vancomycin, Proc. Est. Acad. Sci. 68 (2019) 185–190.

[38] R. Rahmani, M. Antonov, L. Kollo, Y. Holovenko, K.G. Prashanth, Mechanical Behavior of Ti6Al4V Scaffolds Filled with $CaSiO_3$ for Implant Applications, Appl. Sci. 9 (2019) 3844.

[39] N. Kamboj, M. Aghayan, C.S. Rodrigo-Vazquezc, M.A. Rodríguez, I. Hussainova, Novel silicon-wollastonite based scaffolds for bone tissue engineering produced by selective laser melting, Ceram. Int. 45 (2019) 24691–24701.

[40] N. Kamboj, J. Kazantseva, R. Rahmani, M.A. Rodríguez, I. Hussainova, Selective laser sintered bio-inspired silicon-wollastonite scaffolds for bone tissue engineering, Mater. Sci. Eng. C 116 (2020) 111223.

[41] C.S. Rodrigo-Vázquez, N. Kamboj, M. Aghayan, A. Sáez, A.H.D. Aza, M.A. Rodríguez, I. Hussainova, Manufacturing of Silicon-Bioactive glass scaffolds by selective laser melting for bone tissue engineering, Ceram. Int. 46 (2020) 26936–26944.

[42] C.S. Rodrigo-Vázquez, M.A. Rodríguez, A.H. De Aza, Devitrification study of a novel bioactive glass designed on the $CaSiO_3$-$Ca_3(PO_4)_2$-$MgCa(SiO_3)_2$ system, J. Non Cryst. Solids 528 (2020) 119705.

[43] A. Knaislová, P. Novák, S. Cygan, L. Jaworska, M. Cabibbo, High-Pressure Spark Plasma Sintering (HP SPS): a Promising and Reliable Method for Preparing Ti-Al-Si Alloys, Materials (Basel) 10 (2017) 465.

[44] V. Mamedov, Spark plasma sintering as advanced PM sintering method, Powder Metall. 45 (2002) 322–328.

[45] http://www.fct-systeme.de/en (accessed on 20 April 2021).

[46] M. Antonov, R. Veinthal, D.L. Yung, D. Katusin, I. Hussainova, Mapping of impact abrasive wear performance of WC-Co cemented carbides, Wear 332-333 (2015) 971–978.

[47] R. Rahmani, M. Antonov, K.G. Prashanth, The impact resistance of highly densified metal alloys manufactured from gas-atomized pre-alloyed powders, Coatings 11 (2021) 216.

[48] R. Rahmani, M. Brojan, M. Antonov, K.G. Prashanth, Perspectives of metal-diamond composites additive manufacturing using SLM-SPS and other techniques for increased wear-impact resistance, Int. J. Refract. Met. Hard Mater 88 (2020) 105192.

[49] Y. Holovenko, L. Kollo, M. Saarna, R. Rahmani, T. Soloviova, M. Antonov, K.G. Prashanth, S. Cygan, R. Veinthal, Effect of lattice surface treatment on performance of hardmetal-titanium interpenetrating phase composites, Int. J. Refract. Metals Hard Mater. 86 (2020) 105087.

[50] R. Rahmani, M. Brojan, M. Antonov, Lightweight 3D printed Ti6Al4V-AlSi10Mg hybrid composite for impact resistance and armor piercing shielding, J. Mater. Res. Technol. 9 (2020) 13842–13854.

[51] R. Rahmani, M. Antonov, L. Kollo, Selective Laser Melting of Diamond-Containing or Postnitrided Materials Intended for Impact-Abrasive Conditions: experimental and Analytical Study, Adv. Mater. Sci. Eng. (2019) 4210762.

[52] R. Rahmani, M. Antonov, L. Kollo, Wear Resistance of (Diamond-Ni)-Ti6Al4V Gradient Materials Prepared by Combined Selective Laser Melting and Spark Plasma Sintering Techniques, Adv. Tribol. (2019) 5415897.

[53] V.Sh. Sufiiarov, A.A. Popovich, E.V. Borisov, I.A. Polozov, D.V. Masaylo, A.V. Orlov, The Effect of Layer Thickness at Selective Laser Melting, Procedia Eng. 174 (2017) 126–134.

[54] N. Kamboj, A. Ressler, I. Hussainova, Bioactive Ceramic Scaffolds for Bone Tissue Engineering by Powder Bed Selective Laser Processing: a Review, Materials (Basel) 14 (2021) 5338.

[55] E.B. Montufar, M. Casas-Luna, M. Horynová, S. Tkachenko, Z. Fohlerová, S. Diaz-De-La-Torre, K. Dvořák, L. Čelko, J. Kaiser, High strength, biodegradable and cytocompatible alpha tricalcium phosphate-iron composites for temporal reduction of bone fractures, Acta Biomater. 70 (2018) 293–303.

[56] R. Rahmani, K. Molan, M. Brojan, K.G. Prashanth, D. Stopar, High virucidal potential of novel ceramic–metal composites fabricated via hybrid selective laser melting and spark plasma sintering routes, Int. J. Adv. Manuf. Technol. (2022) 1–14.

[57] K. Molan, R. Rahmani, D. Krklec, M. Brojan, D. Stopar, Phi 6 Bacteriophage Inactivation by Metal Salts, Metal Powders, and Metal Surfaces, Viruses 14 (2022) 204.